physica status solidi a
www.pss-a.com

Coating of Self-Sensing Atomic Force Microscopy Cantilevers with Boron-Doped Nanocrystalline Diamond at Low Temperatures

Štěpán Potocký, Jaroslav Kuliček, Egor Ukraintsev, Ondřej Novotný, Alexander Kromka, and Bohuslav Rezek*

Doped diamond has found a commercial use for achieving durable and reproducible electrical measurements in atomic force microscopy (AFM). Yet so far it has not been used on self-sensing AFM probes due to thermally and mechanically sensitive integrated detection circuits. Herein, conventional microwave plasma chemical vapor deposition (CVD) is employed while taking advantage of thermal conductivity along the silicon AFM cantilever probe for growing high-quality B-doped nanocrystalline diamond film on the probe apex that is selectively seeded by dip coating in nanodiamond solution. By investigating various CVD process parameters, it is shown that the detection circuit remains functional up to 400 °C for 2 h deposition or up to 8 h at 300 °C. Scanning electron microscopy and Raman spectroscopy corroborate quality of the diamond coating and doping. The self-sensing probes are successfully tested in conductive AFM (C-AFM) regime and surface spreading resistance regime, showing linear response in current–voltage spectroscopy and capability of conductivity mapping on metals and semiconductor devices. In the results, prospects for stable C-AFM measurements when conventional optical detection is not suitable, such as on photosensitive materials or in probe-electron microscopy, are opened.

1. Introduction

Atomic force microscopy (AFM) has become an indispensable tool in nanotechnology, enabling high-resolution imaging and measurement of surface properties at the nanoscale. The performance of AFM probes is critically dependent on the properties of the AFM tips. A typical essential requirement for AFM tips is a combination of mechanical robustness, chemical inertness, and thermal stability to meet rigorous demands of various applications.[1] Diamond's superior properties[2] can significantly enhance the mechanical durability of AFM probes, which is particularly beneficial for prolonged use in harsh environments and high-resolution imaging. Additionally, diamond's chemical inertness makes it resistant to a wide range of corrosive environments, a property crucial for AFM applications involving biological samples and other chemically aggressive conditions.[3] High thermal conductivity of diamond is considered beneficial for high-speed AFM scanning and thermal analysis applications.[4,5] Furthermore, by using doped diamond as bulk or as coatings, electrical conductivity of the AFM tips can be tailored to specific applications while providing mechanical durability at the same time. Conductive diamond tips have become essential for various scanning probe techniques, including conductive or electrochemical AFM analyses.[6–9]

In previous decades, diamond AFM tips were fabricated through various methods, including direct chemical vapor deposition (CVD)[10] on Si tips,[11,12] reactive ion etching of diamond,[13,14] or using micromachined molds.[15–18] However, these approaches have two main drawbacks—1) the high-temperature loading of the AFM tip during the CVD of diamond, typically reaching 800 °C and 2) the complexity of the fabrication process.

For conventional AFM measurements, optical detection employing LED or laser beam deflection on a cantilever probe has become the most commonly employed method. Complementary to this, self-sensing AFM probes have been developed to enable a direct and efficient measurement in vacuum or environments where illumination represents an

Š. Potocký, J. Kuliček, E. Ukraintsev, B. Rezek
Faculty of Electrical Engineering
Czech Technical University in Prague
Technická 2, 16627 Prague, Czechia
E-mail: potocste@fel.cvut.cz

A. Kromka
Institute of Physics
Czech Academy of Sciences
Cukrovarnická 10, 16200 Prague, Czechia

O. Novotný
NenoVision s.r.o.
Purkyňova 649, 61200 Brno, Czechia

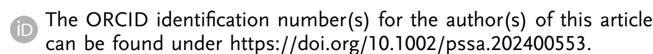
The ORCID identification number(s) for the author(s) of this article can be found under https://doi.org/10.1002/pssa.202400553.

© 2024 The Author(s). physica status solidi (a) applications and materials science published by Wiley-VCH GmbH. This is an open access article under the terms of the Creative Commons Attribution License, which permits use, distribution and reproduction in any medium, provided the original work is properly cited.

DOI: 10.1002/pssa.202400553

obstacle.[19] These probes offer a promising alternative to the conventional optical AFM detection methods, for example, when an AFM module is integrated with scanning electron microscopy (SEM) for correlative probe-electron microscopy.[20,21] Among the large variety of AFM modes, conductive tips are necessary for diverse electrical modes such as conductive AFM (C-AFM), Kelvin probe force microscopy, piezoresponse force microscopy, surface spreading resistance microscopy (SSRM), and current–voltage (I–V) spectroscopy analyses. Doped diamond has already been found to be instrumental and in demand for achieving durable and reproducible electrical measurements in AFM.[22] However, it has not been explored for self-sensing AFM cantilevers so far due to many technological obstacles. A critical challenge is the integrated metal-based detection circuit with the Wheatstone bridge, which becomes nonconductive during the high-temperature CVD process. Although boron-doped diamond growth is possible at lower temperatures, it still presents several technological challenges.[23–25]

In this work, we present a novel approach for selective apex coating of self-sensing AFM cantilevers with boron-doped nanocrystalline diamond (BNCD) films at reduced deposition temperatures. This method successfully maintains the functionality of the integrated Al-based detection circuit while simultaneously providing high-quality conductive BNCD film on the tip. We demonstrate the full functionality of these self-sensing AFM probes for various electrical AFM modes.

2. Experimental Section

Thin BNCD films were grown on conductive self-sensing silicon-based AFM cantilevers of $2 \times 3\,mm^2$ (NenoProbe Conductive, NenoVision s.r.o., Czechia). Before the CVD growth, substrates were pretreated in a suspension of deionized water and ultra-dispersed detonation diamond powder (ø5 nm, New Metals and Chemicals Corp. Ltd., Kyobashi).[26]

To prevent short-circuiting of the existing Wheatstone bridge and contacts, the conductive diamond layer was selectively deposited only at the apex of the AFM probe. A selected-area deposition utilizing selective-area seeding (i.e., nucleation) by detonation nanodiamonds was adapted for this purpose.[27] Detonation diamond powder was deposited on a tip apex by dipping the AFM cantilever front part (≈300 µm) into a droplet containing the seeding suspension. This procedure was accomplished by using a custom-made mechanical dipping apparatus which consisted of a spring-loaded holder for the AFM probe and a micrometer screw to precisely dip the cantilever into the seeding solution. This approach ensures accurate and reproducible deposition of the diamond nanoparticles on the desired areas of the self-sensing Si AFM probe.

The CVD deposition of BNCD was performed in a microwave plasma-enhanced multimode clamshell cavity reactor system (SEKI SDS6K, Cornes Technologies, Ltd.). The constant process parameters were 5% CH_4 of the H_2/CH/TMB gas mixture (TMB: trimethylborate), a total gas flow rate of 200 sccm, a chamber pressure of 4 kPa (30 Torr), and a B/C ratio of 10 000 ppm. The crucial varied parameter in our study was the substrate temperature (T_s) due to the presence of self-sensing structures on the Si cantilever. The T_s was measured through a side window with a dual-wavelength pyrometer (200–600 °C, PRO 92-20-C-23, Williamson) focused on the tip of the AFM cantilever. It was adjusted to 300, 350, and 400 °C by microwave (MW) power 1, 2, and 3 kW, respectively. A fine T_s adjustment was achieved by tuning the heat removal from the sample holder using plenum pressure. As the diamond deposition is a temperature-controlled process,[10] the CVD growth time was fixed at 8 h for $T_s = 300$ °C (sample S1), 4 h for $T_s = 350$ °C (sample S2), and 2 h for $T_s = 400$ °C (sample S3), see **Table 1**.

Surface morphology of the samples was obtained by SEM (Zeiss EVO 10). The SEM images were acquired at 10 kV at a working distance of 10 mm and magnifications 41 X to 20 kX in the secondary electrons (SE) regime using an off-beam detector. The material and chemical composition were determined using the confocal Raman microscope (WITec *alpha300* RAS) equipped with a green light laser (excitation wavelength 532 nm, laser power 2 mW). Raman spectra were collected by 100x objective (NA 0.9) and UHTS 300 spectrometer with the 1800 g mm^{-1} grating. The 5 min integration time was constant for all acquisitions and the spectra were averaged from two acquisitions. Spectra were recorded from several positions on the AFM cantilever. Spectra were collected and processed by WITec Control 6.1 and WITec Project 6.1 software. Electrical characterization of the Wheatstone bridge functionality was performed using a probe station (SM-1A, Measure Jig Co.) connected to a multimeter (SMU2401, Keithley). The AFM measurements were conducted using LiteScope AFM (NenoVision s.r.o., Czech Republic), designed for easy integration into SEMs, enabling simultaneous acquisition of AFM and SEM data and their straightforward correlation. Conductivity measurements with a diamond tip were performed in both atmospheric and vacuum conditions with the biased tip.

Table 1. Table of differing growth process parameters and electrical performance of Wheatstone bridge before and after BNCD deposition on self-sensing AFM cantilevers.

Sample	Growth process parameters				Electrical properties before/after BNCD growth			
	MW power [W]	Plenum [kPa]	Growth temperature [°C]	Growth time [h]	R1 [kΩ]	R2 + R3 [kΩ]	R4 [kΩ]	Leakage [GΩ]
S1	1000	0.9	300	8	4.6/15.6[a]	14.6/49.6[a]	5.0/18.2[a]	>1/>1[a]
S2	2000	2.0	350	4	4.2/5.7[a]	11.1/17.7[a]	3.7/6.9[a]	>1/>1[a]
S3	3000	1.6	400	2	7.2/18.5[a]	16.3/48.8[a]	5.5/16.6[a]	>1/>1[a]

[a]Values before/after BNCD deposition.

© 2024 The Author(s). physica status solidi (a) applications and materials science published by Wiley-VCH GmbH

18626319, 2025, 5, Downloaded from https://onlinelibrary.wiley.com/doi/10.1002/pssa.202400553 by Cochrane Czech Republic, Wiley Online Library on [12/03/2025]. See the Terms and Conditions (https://onlinelibrary.wiley.com/terms-and-conditions) on Wiley Online Library for rules of use; OA articles are governed by the applicable Creative Commons License

18626319, 2025, 5, Downloaded from https://onlinelibrary.wiley.com/doi/10.1002/pssa.202400553 by Cochrane Czech Republic, Wiley Online Library on [12/03/2025]. See the Terms and Conditions (https://onlinelibrary.wiley.com/terms-and-conditions) on Wiley Online Library for rules of use; OA articles are governed by the applicable Creative Commons License

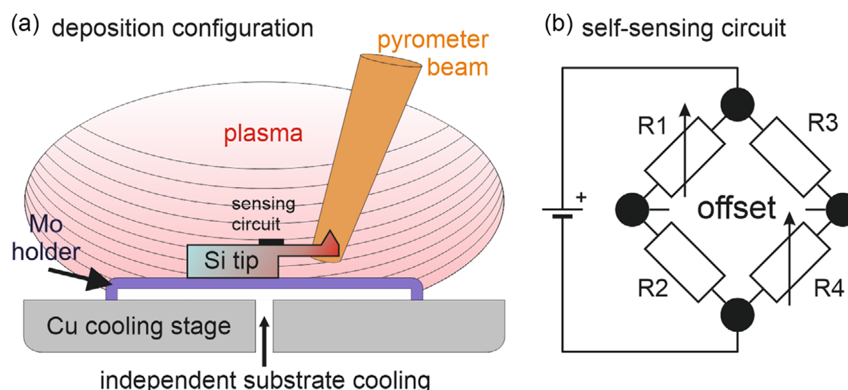

Figure 1. Schematic view of a) the experimental setup during the selected area diamond CVD growth and b) the Wheatstone bridge circuit of the self-sensing AFM probe.

3. Results and Discussion

Figure 1a shows the schematic view of the experimental setup in the plasma CVD chamber. The pyrometer field of view is 5 mm in diameter, enabling precise positioning of the beam on the AFM probe in the CVD chamber. The scheme shows the situation where the pyrometer laser aim is directed to the tip. Although the pyrometer collects the signal from larger area, the most relevant contribution is from the tip which has the highest temperature.

The critical parameter for the successful deposition is the substrate temperature T_s. For $T_s > 500\,°C$, we observed the degradation of the Wheatstone bridge circuit. The T_s is determined by the balance between heating from the plasma source and thermal conduction to the cooling substrate stage. The thermal conductivity is adjusted by the independently controlled plenum pressure in the cavity volume between the Cu cooling stage and the Mo substrate holder. The pyrometer field of view is 5 mm in diameter, enabling precise positioning on the AFM probe in the CVD chamber. It helped us identify different temperatures on the AFM tip and body (lower by $\approx$ 100 °C). Such a high-temperature gradient along the cantilever can be advantageous for the selective area deposition.[28] The BNCD growth is thereby initiated, and limited, on the seeded area, whereas low T_s suppresses the parasitic growth on the body of the AFM probe.[29]

Figure 1b shows the Wheatstone bridge circuit on the self-sensing AFM probe. The R1 and R4 correspond to piezoresistive (active) elements at the base of the cantilever with values of 2–10 kΩ. The R2 and R3 correspond to a reference element on the silicon body with values of 2–10 kΩ. Changes in the resistance $>$100 kΩ are considered as a probe malfunction. Leakage resistance between the circuit and the tip contact is $>$2 MΩ (typically above GΩ), and after the deposition it should not be $<$1 MΩ.

Figure 2 shows representative SEM images of the AFM probe after BNCD deposition from the perspective of the whole self-sensing probe (Figure 2a), selective area deposition (Figure 2b), the tip (Figure 2c), and tip apex (Figure 2d) for the CVD deposition at the highest $T_s = 400\,°C$ (sample S3). SEM analyses for the samples S1 and S2 are shown in Figure S2, Supporting Information.

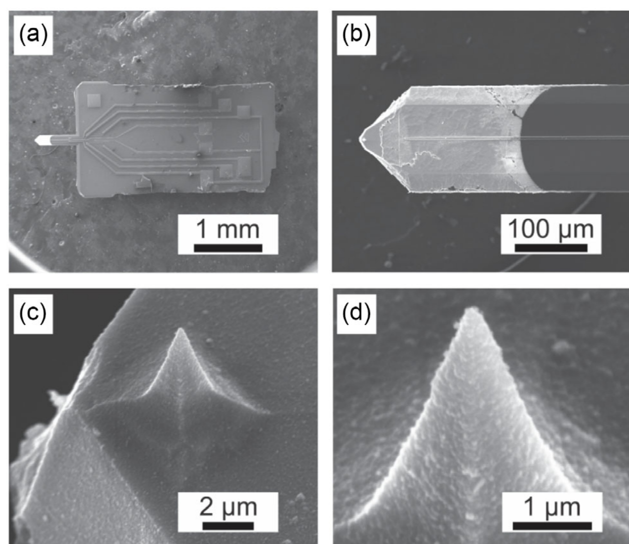

Figure 2. Representative SEM images of the AFM probe after BNCD deposition from the perspective of a) the whole self-sensing probe, b) selective area deposition, c) the tip, and d) tip apex for the $T_s = 400\,°C$ (sample S3).

Figure 2a shows a low magnification SEM image of the whole AFM probe, revealing rectangular contact pads with the paths leading to the self-sensing bridge located in the first quarter of the cantilever. Careful inspection of the electrical contact did not reveal any damage or short circuit caused by BNCD, as also confirmed by the electrical measurements (Table 1). The white area of the cantilever corresponds to the BNCD film, exhibiting high contrast in the SE regime due to the higher secondary electron yield of diamond compared to non-diamond material.[30] Figure 2b provides a detailed view of this area, showing the morphology of the BNCD-overgrown electrical contact. The concave profile of the BNCD film corresponds to the seeded area, resulting from the surface tension of the water-based seeding solution into which the tip was dipped.

A fully closed homogenous BNCD coating on the cantilever tip is observed in Figure 2c. Figure 2d shows the uniform nanocrystalline character of the BNCD film on the tip apex of the

© 2024 The Author(s). physica status solidi (a) applications and materials science published by Wiley-VCH GmbH

self-sensing probe. The entire tip area, including tip edges and apex, is covered with the homogenous BNCD layer. Figure S1, Supporting Information, shows the SEM cross section (cut by Xe-plasma-focused ion beam) of the AFM tip after the BNCD layer growth for 12 h at $T_s \approx 350$ °C. The cross section shows conformal uniform coating of the tip apex. The BNCD thickness can be estimated to ≈500 nm. The BNCD coating thickness on the sample S2 can be thus estimated to be about ≈150 nm, as the deposition time was 3× shorter (4 h). We did not perform testing of the tip diameter on a test specimen in AFM as the SEM analyses provide more straightforward visual information.

Raman spectroscopy was employed to confirm the presence of BNCD in seeded area and its absence in unseeded areas. **Figure 3** shows Raman spectra of BNCD coatings from three distinctive regions (as denoted in Figure 3a) for the samples S1–S3 (Figure 3b–d) as a function of deposition temperature and time. The red curve represents the measurement of the BNCD on the AFM tip, the green curve represents the measurement of the BNCD on the cantilever adjacent to the AFM tip, and the blue curve represents the measurement of unseeded cantilever area (i.e., without BNCD coating). Characteristic peaks corresponding mainly to Si substrate, diamond, and boron are identified in the Raman spectra. The characteristic diamond peak centered at 1332 cm^{-1} is accompanied by the broad bands at 500 and 1220 cm^{-1}, which correspond to the boron presence in the BNCD.[9,23] The low wavenumber BNCD peak overlaps with the sharp 520 cm^{-1} from the monocrystalline Si substrate. The broad band at around 980 cm^{-1} is attributed to the second order of silicon. Additionally, the broad band at 1470 cm^{-1} is typically associated with the nanocrystalline diamond band at 1130 cm^{-1}.[24]

For all samples, the most distinct diamond peak (1332 cm^{-1}) is measured from the selective growth area on the cantilever apex. The intensity of this peak decreased on the tip area, which could indicate a reduced film thickness[31] yet most likely it is due to Raman focus volume. Similarly, boron doping band intensity is affected correspondingly (a fixed nominal doping level was used for all the samples). The intensities of nanocrystalline diamond bands decrease with the increasing T_s, which is consistent with growth kinetics and temperature-dependent growth processes. No diamond peak was detected outside the seeded area, confirming the absence of parasitic diamond growth.

Table 1 summarizes the selected growth process parameters and electrical characteristics of the self-sensing AFM probe before and after the BNCD deposition. The electrical structures ensuring the self-sensing capability degrade at temperatures above 500 °C, particularly for extended growth process times. After the CVD growth process, similar changes in electrical properties were observed for the S1 and S3 probes, both somewhat higher than for S2 probe. Comparing changes for the S1 and S3

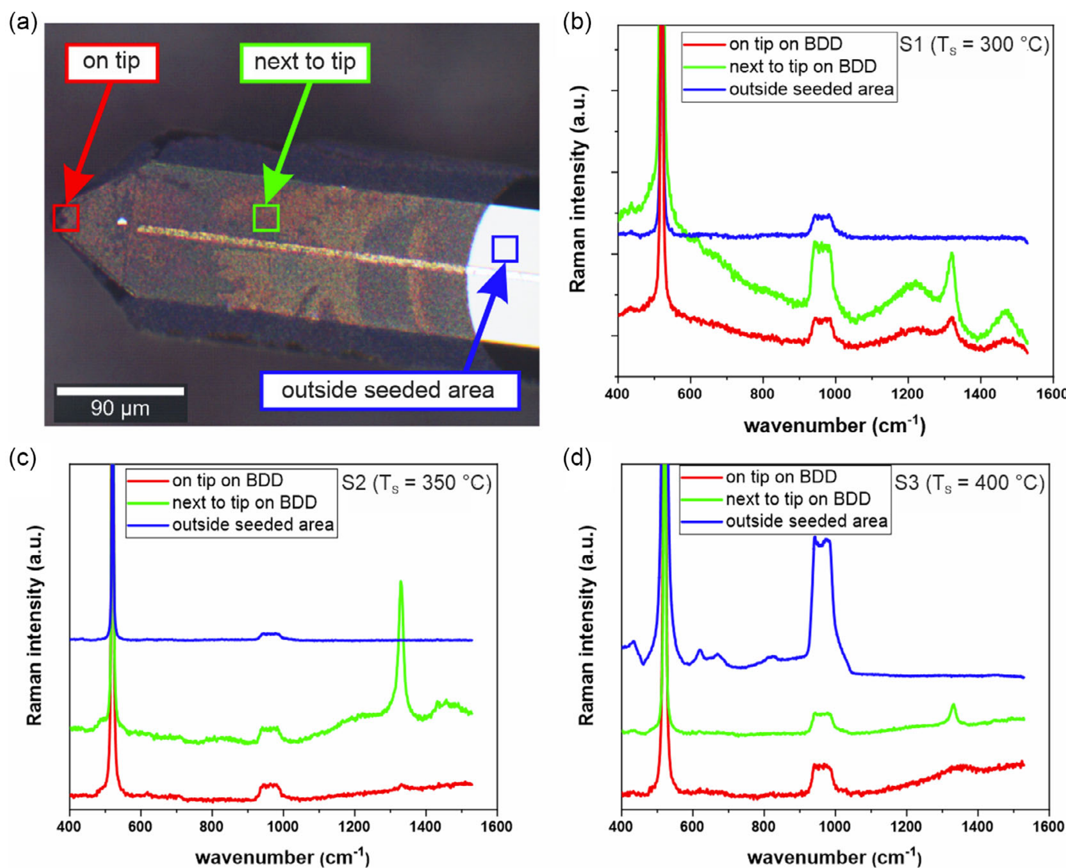

Figure 3. a) Typical optical microscope image of a cantilever with the selectively grown diamond layer with three denoted areas where Raman spectra (532 nm excitation) were measured on the samples b) S1, c) S2, and d) S3 (growth temperature T_s = 300, 350, and 400 °C, respectively).

© 2024 The Author(s). physica status solidi (a) applications and materials science published by Wiley-VCH GmbH

18626319, 2025, 5, Downloaded from https://onlinelibrary.wiley.com/doi/10.1002/pssa.202400553 by Cochrane Czech Republic, Wiley Online Library on [12/03/2025]. See the Terms and Conditions (https://onlinelibrary.wiley.com/terms-and-conditions) on Wiley Online Library for rules of use; OA articles are governed by the applicable Creative Commons License

probes suggests an interaction between two opposing parameters: substrate temperature and deposition time. Higher substrate temperature T_s is a critical parameter for the degradation of Al metallization, while prolonged deposition times exacerbate this effect even for temperatures below 500 °C.

The balance between all the bridge resistors is critical for self-sensing functionality. During the self-sensing AFM measurements, it must be possible to compensate the bridge offset V_{offset} by leveling one of the bridge outputs. Based on the instrumentation amplification mechanism and bridge power supply V_{in}, this creates limits for resistors balance. In our instrumentation, the conditions give us limitation $V_{offset} \leq 0.2 \times V_{in}$ where probes outside these values cannot be compensated, and hence, rendering such self-sensing probes unusable. All samples exhibited values of R1, R2, R3, and R4 < 100 kΩ and resistance balance ≤ 0.2, and the leakage resistance > 1 GΩ. Thus, they passed the established electrical validation test before proceeding with further assembly steps.

The BNCD-coated AFM self-sensing probes were then fixed and wire bonded on a holder for C-AFM measurements. **Figure 4**a,b shows examples of *I–V* curves obtained in the C-AFM regime and SSRM regime using the S3 probe on a gold test grid sample. The S3 probe was selected for this case study due to its practical short deposition time and highly crystalline yet thin coating (as evidenced by the SEM and Raman analyses), while maintaining good self-sensing parameters. The obtained *I–V* curves exhibit smooth linear profiles and without any hysteresis in both regimes. The contact resistance is ≈21 MΩ providing a solid foundation for C-AFM and SSRM applications.

To verify the performance, AFM scanning experiments were conducted using standard settings: scan speed of 20 μm s^{-1}, tip bias voltage of 0.5 V, 1 MΩ resistor in series for current surge protection, and a force setpoint of 0.01 V (corresponding to about 800 nN). Figure 4c shows the AFM surface topography and C-AFM map of electrical currents on the gold test grid, obtained by scanning the surface with the S3 probe using the aforementioned parameters. The topography map reveals a flat surface with trenches between the square features on the test grid. The test grid intentionally includes a 2 × 2 set of middle squares electrically isolated, clearly resolved in the C-AFM map. The conductive squares exhibit an overall smooth current image at around 20 nA with scattered low conductive (dark) dots, most likely corresponding to scratches and impurities, consistent with typical observations on gold test layers. This measurement demonstrates successful reproducible C-AFM imaging with self-sensing cantilevers with BNCD on the apex.

Figure 5 shows C-AFM electrical map of 3D Nand device with polysilicon channels and nonconductive cores with 200 nm diameter. The image was taken in SEM which was used for precise navigation to the region of interest. Scanning parameters were scan speed of 20 μm s^{-1}, tip bias voltage of 9 V, and a force setpoint of 0.05 V (corresponding to about 4 μN). The C-AFM map reveals the donut shape structure of the channels with good lateral resolution and two different types of channels, one with a current of 20 pA and the second with currents above 400 pA. From the image, we could estimate the resolution in C-AFM regime below 50 nm. The Figure S1, Supporting Information, shows the obvious: BCND coating makes the tip diameter larger, which may affect the AFM spatial resolution morphology and

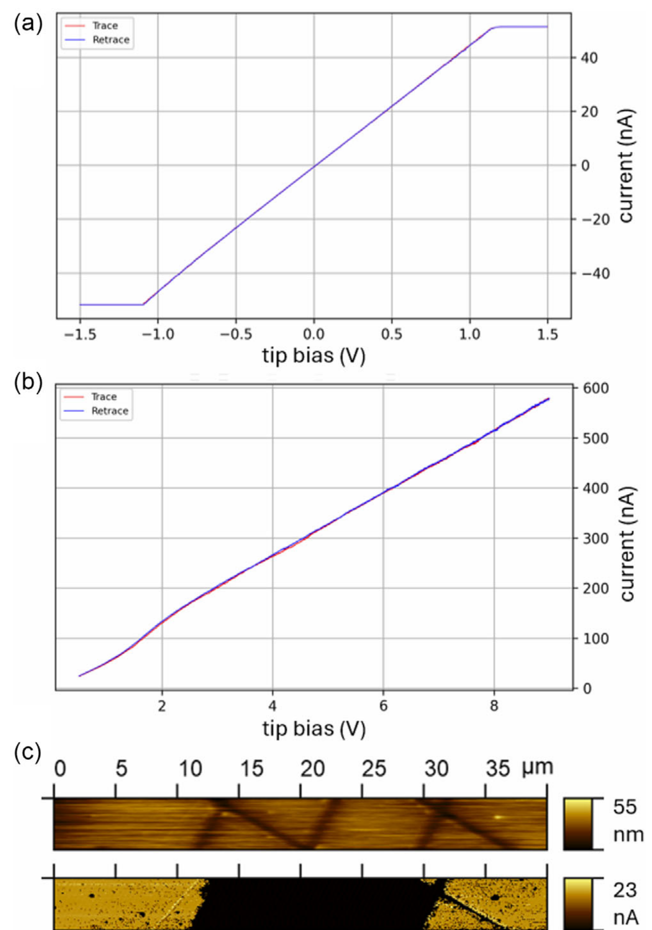

Figure 4. *I–V* curves obtained in a) conductive AFM regime (C-AFM) and b) surface spreading resistance microscopy (SSRM) regime with the BNCD-coated S3 self-sensing probe on a gold test grid. c) AFM surface topography and C-AFM map of electrical currents on the gold test grid, obtained by scanning the surface with the BNCD-coated S3 self-sensing probe. Central squares are intentionally designed as electrically insulating.

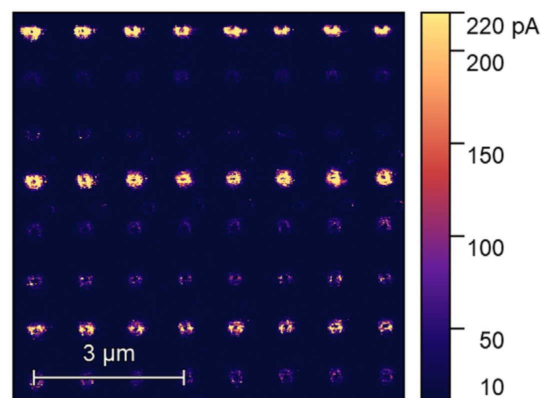

Figure 5. Microscopic C-AFM map of electrical currents on a surface of 3D Nand device with polysilicon channels and nonconductive cores with 200 nm diameter.

© 2024 The Author(s). physica status solidi (a) applications and materials science published by Wiley-VCH GmbH

18626319, 2025, 5, Downloaded from https://onlinelibrary.wiley.com/doi/10.1002/pssa.202400553 by Cochrane Czech Republic, Wiley Online Library on [12/03/2025]. See the Terms and Conditions (https://onlinelibrary.wiley.com/terms-and-conditions) on Wiley Online Library for rules of use; OA articles are governed by the applicable Creative Commons License

current. But generally it will depend also on the particular type of sample and its surface morphology. Comparison of C-AFM resolution with standard self-sensing tips could be done as they have no such electrical connection. Available metal-coated self-sensing tips do not provide sufficient robustness and durability. In our experience, the metal coating quickly wears off in contact mode and although some conductivity can be retained, the current and shape are changing. Comparison would be thus ambiguous.

4. Conclusion

The study demonstrated successful application of low-temperature microwave plasma CVD process and selective nanodiamond seeding for the growth of high-quality BNCD coating on the apex of self-sensing AFM probes. It was possible to maintain the functionality of an integrated Al-based Wheatstone detection circuit, which typically becomes nonconductive or leaky when processed at substrate temperatures exceeding 500 °C. Electrical characterization of the Wheatstone detection circuit confirmed its functionality up to $T_s = 400$ °C within 2 h deposition time. At lower T_s values of 300 °C, the deposition time can be prolonged up to 8 h without circuit degradation. At the same time, SEM and Raman analyses confirmed the growth of conformal, homogenous BNCD coating (up to 500 nm thickness) on the cantilever tip at substrate temperatures as low as $T_s = 300$ °C. An important role was played by the thermal conductivity effect when the AFM cantilever tip was heated in CVD plasma considerably higher (by 100 °C) than the rest of the chip. Moreover, the low-temperature growth regime combined with the selective area seeding effectively suppressed parasitic BNCD growth, preventing shortcuts in the self-sensing circuit. Full functionality of the self-sensing C-AFM regime was demonstrated by local I–V spectroscopy and electrical current mapping on metal layers and semiconductor nanodevices. These results open prospects for durable conductive AFM experiments using self-sensing cantilevers in SEM or in general where AFM with conventional optical detection is unsuitable such as analyses of photovoltaic, photocatalytic, plasmonic materials, or measurements in opaque liquids.

Supporting Information

Supporting Information is available from the Wiley Online Library or from the author.

Acknowledgements

This publication was supported by the Technology Agency of the Czech Republic through project TM03000033 (TACOM) and the project CZ.02.01.01/00/22_008/0004596 (SenDISo) under the Operational Program Johannes Amos Commenius, call for Excellent Research. The authors gratefully acknowledge the kind assistance of Tescan a.s. with the cross-sectional analysis using the Xe plasma FIB SEM system AmberX. The authors also kindly acknowledge discussions about the self-sensing probe design with Paweł Janus from Łukasiewicz Institute of Microelectronics and Photonics.

Open access publishing facilitated by Ceske vysoke uceni technicke v Praze, as part of the Wiley - CzechELib agreement.

Conflict of Interest

The authors declare no conflict of interest.

Data Availability Statement

The data that support the findings of this study are openly available in [Zenodo] at [https://doi.org/10.5281/zenodo.12654928], reference number [12654928].

Keywords

boron-dopings, conductive atomic force microscopies, microwave plasma chemical vapor deposition, nanocrystalline diamonds, self-sensing probes

Received: July 8, 2024
Revised: September 11, 2024
Published online: October 1, 2024

[1] P. C. Fletcher, J. R. Felts, Z. Dai, T. D. Jacobs, H. Zeng, W. Lee, P. E. Sheehan, J. A. Carlisle, R. W. Carpick, W. P. King, *ACS Nano* **2010**, *4*, 3338.
[2] C. E. Nebel, *Nat. Mater.* **2003**, *2*, 431.
[3] C. E. Nebel, B. Rezek, D. Shin, H. Uetsuka, N. Yang, *J. Phys. D: Appl. Phys.* **2007**, *40*, 6443.
[4] W. P. King, B. Bhatia, J. R. Felts, H. J. Kim, B. Kwon, B. Lee, S. Somnath, M. Rosenberger, *Annu. Rev. Heat Transfer* **2013**, *16*, 287.
[5] O. D. Payton, L. Picco, T. B. Scott, *Int. Mater. Rev.* **2016**, *61*, 473.
[6] T. Hantschel, P. Niedermann, T. Trenkler, W. Vandervorst, *Appl. Phys. Lett.* **2000**, *76*, 1603.
[7] C. Kranz, *Electroanalysis* **2016**, *28*, 35.
[8] S. Daboss, P. Knittel, C. E. Nebel, C. Kranz, *Small* **2019**, *15*, 1902099.
[9] R. Bogdanowicz, M. Sobaszek, M. Ficek, D. Kopiec, M. Moczała, K. Orłowska, M. Sawczak, T. Gotszalk, *Appl. Phys. A* **2016**, *122*, 270.
[10] M. Schwander, K. Partes, *Diam. Relat. Mat.* **2011**, *20*, 1287.
[11] Ph. Niedermann, W. Hänni, N. Blanc, R. Christoph, J. Burger, *J. Vac. Sci. Technol. A: Vac. Surf. Films* **1996**, *14*, 1233.
[12] M. M. Huang, D. W. Zuo, W. Z. Lu, F. Xu, M. Wang, *Key Eng. Mater.* **2010**, *431–432*, 499.
[13] T. Shibata, K. Maruno, M. Nagai, T. Kawashima, T. Mineta, E. Makino, *Key Eng. Mater.* **2012**, *523–524*, 569.
[14] H. Uetsuka, T. Yamada, S. Shikata, *Diam. Relat. Mat.* **2008**, *17*, 728.
[15] T. Shibata, T. Nakatsuji, Y. Kitamoto, K. Unno, E. Makino, in *Proc. SPIE 3680, Design, Test, and Microfabrication of MEMS and MOEMS* (Eds: B. Courtois, S. B. Crary, W. Ehrfeld, H. Fujita, J. M. Karam, K. W. Markus), Paris, France, March **1999**, p. 1125, https://doi.org/10.1117/12.341185.
[16] J. W. Park, D. W. Lee, N. Takano, N. Morita, *Mater. Sci. Forum* **2006**, *505–507*, 79.
[17] T. Hantschel, M. Tsigkourakos, J. Kluge, T. Werner, L. Zha, K. Paredis, P. Eyben, T. Nuytten, Z. Xu, W. Vandervorst, *Microelectron. Eng.* **2015**, *141*, 1.
[18] T. Shibata, Y. Kitamoto, K. Unno, E. Makino, *J. Microelectromech. Syst.* **2000**, *9*, 47.
[19] G. E. Fantner, W. Schumann, R. J. Barbero, A. Deutschinger, V. Todorov, D. S. Gray, A. M. Belcher, I. W. Rangelow, K. Youcef-Toumi, *Nanotechnology* **2009**, *20*, 434003.
[20] D. Rutherford, K. Kolářová, J. Čech, P. Haušild, J. Kuliček, E. Ukraintsev, Š. Stehlík, R. Dao, J. Neuman, B. Rezek, *Ultramicroscopy* **2024**, *258*, 113909.

© 2024 The Author(s). physica status solidi (a) applications and materials science published by Wiley-VCH GmbH

18626319, 2025, 5, Downloaded from https://onlinelibrary.wiley.com/doi/10.1002/pssa.202400553 by Cochrane Czech Republic, Wiley Online Library on [12/03/2025]. See the Terms and Conditions (https://onlinelibrary.wiley.com/terms-and-conditions) on Wiley Online Library for rules of use; OA articles are governed by the applicable Creative Commons License

[21] I. W. Rangelow, M. Kaestner, T. Ivanov, A. Ahmad, S. Lenk, C. Lenk, E. Guliyev, A. Reum, M. Hofmann, C. Reuter, M. Holz, *J. Vac. Sci. Technol. B* **2018**, *36*, 06J102.
[22] W. Smirnov, A. Kriele, R. Hoffmann, E. Sillero, J. Hees, O. A. Williams, N. Yang, C. Kranz, C. E. Nebel, *Anal. Chem.* **2011**, *83*, 4936.
[23] P. Ashcheulov, A. Taylor, Z. Vlčková Živcová, P. Hubík, J. Honolka, M. Vondráček, M. Remzová, J. Kopeček, L. Klimša, J. Lorinčik, M. Davydova, Z. Remeš, M. Kohout, A. M. Beltran, V. Mortet, *Appl. Mater. Today* **2020**, *19*, 100633.
[24] M. Sobaszek, Ł. Skowroński, R. Bogdanowicz, K. Siuzdak, A. Cirocka, P. Zięba, M. Gnyba, M. Naparty, Ł. Gołuński, P. Płotka, *Opt. Mater.* **2015**, *42*, 24.
[25] T. Izak, O. Babchenko, S. Potocky, Z. Remes, H. Kozak, E. Verveniotis, B. Rezek, A. Kromka, in *RSC Nanoscience & Nanotechnology* (Ed: O. A. Williams), Cambridge **2014**, pp. 290–342, ISBN 978-1-84973-639-8.
[26] A. Kromka, š. Potocký, J. Čermák, B. Rezek, J. Potměšil, J. Zemek, M. Vaněček, *Diam. Relat. Mat.* **2008**, *17*, 1252.
[27] O. Babchenko, T. Izak, E. Ukraintsev, K. Hruska, B. Rezek, A. Kromka, *Phys. Status Solidi B: Basic Solid State Phys.* **2010**, *247*, 3026.
[28] J. E. Butler, Y. A. Mankelevich, A. Cheesman, J. Ma, M. N. R. Ashfold, *J. Phys.: Condes. Matter* **2009**, *21*, 364201.
[29] O. Babchenko, E. Verveniotis, K. Hruska, M. Ledinsky, A. Kromka, B. Rezek, *Vacuum* **2012**, *86*, 693.
[30] A. Shih, J. Yater, P. Pehrsson, J. Butler, C. Hor, R. Abrams, *J. Appl. Phys.* **1997**, *82*, 1860.
[31] R. S. Das, Y. K. Agrawal, *Vib. Spectrosc.* **2011**, *57*, 163.

© 2024 The Author(s). physica status solidi (a) applications and materials science published by Wiley-VCH GmbH

18626319, 2025, 5, Downloaded from https://onlinelibrary.wiley.com/doi/10.1002/pssa.202400553 by Cochrane Czech Republic, Wiley Online Library on [12/03/2025]. See the Terms and Conditions (https://onlinelibrary.wiley.com/terms-and-conditions) on Wiley Online Library for rules of use; OA articles are governed by the applicable Creative Commons License